Eur. Phys. J. D **18**, 5–13 (2002)
DOI: 10.1140/e10053-002-0001-z

THE EUROPEAN PHYSICAL JOURNAL D
EDP Sciences

Dark-line in optically-thick vapors: inversion phenomena and line width narrowing

A. Godone[1], F. Levi[1,a], S. Micalizio[2], and J. Vanier[3]

[1] Istituto Elettrotecnico Nazionale "Galileo Ferraris", Strada delle Cacce 91, 10135 Torino, Italy
[2] Politecnico di Torino, Corso Duce degli Abruzzi 24, 10124 Torino, Italy
[3] Département de Physique, Université de Montréal, Montréal, QUE Canada

Received 28 March 2001 and Received in final form 3 October 2001

Abstract. An analysis of the phenomenon of coherent population trapping as observed by means of the dark state in the case of optically thick vapors in alkali metal atoms is presented. Very different behaviors are predicted for the observation of the dark state in the fluorescence and transmission spectra of the same atomic sample when the optical length is not negligible. Among other effects, the dark line observed in the fluorescence signal may look inverted appearing as a bright line, while in the transmission signal a narrowing of the line width resonance line is observed for an increase of the atomic density. In the pure three-level scheme a subnatural width is predicted. These effects, related to the electromagnetically induced transparency phenomenon, are readily observed in experiments, which are found to be in excellent agreement with the theory developed.

PACS. 32.80.Wr Other multiphoton processes – 06.30.Ft Time and frequency – 31.15.Ne Self-consistent-field methods – 42.50.Md Optical transient phenomena: quantum beats, photon echo, free-induction decay, dephasings and revivals, optical nutation, and self-induced transparency

1 Introduction

Interference effects in the excitation of an atomic ensemble by means of two coherent radiation fields, in a Λ scheme, have first been observed by Alzetta *et al.* in Na vapors [1]. In that case, and in the study reported here, the Λ scheme couples the two ground state hyperfine levels of the alkali-atoms to a common excited state. The interference effects are due to a coherent superposition of the two ground state hyperfine levels with a π rad dephasing between the respective wavefunctions, a phenomenon known as Coherent Population Trapping (CPT). In particular, a dark line is observed in the fluorescence spectrum of the alkali atoms as well as a bright line in transmission, when the two optical radiation frequency difference is resonant with the hyperfine transition (an Electromagnetically Induced Transparency effect (EIT) [2]). The strong coherence created between the hyperfine levels leads also to coherent microwave emission when the atomic ensemble is placed in a microwave cavity [3,4].

The theory of the above phenomena has been developed, in the case of an optically thin medium [5]. A review of the applications of the CPT phenomenon in the laser spectroscopy field may be found in [6,7]. Other applications of the CPT phenomenon have been proposed in the fields of magnetometry [8], atom cooling [9], "lasing" without inversion [10] and atomic frequency standards [11–13]. Finally non-linear effects in double Λ configurations have been examined in [14] and anomalous dispersion phenomena have been reported in [15]. With reference to the field of atomic frequency standards the intrinsic properties of CPT allow in principle a strong reduction of the light-shift effect as pointed out in [4,5,16]. The use of dark transitions is then particularly suited in the implementation of a compact, low-power frequency standard [13]. However, even if the operating temperature considered for these applications is always below 60 °C for Rb and 40 °C for Cs, density effects are not negligible and the atomic sample cannot be considered optically thin.

In this paper we extend the theory of the dark transitions to an optically thick atomic vapor with buffer gas. Inverted dark lines in the fluorescence spectrum and line width narrowing *versus* atomic density are predicted in the case of optically thick samples in good agreement with the experimental results obtained with ^{87}Rb or ^{133}Cs. The impact of these new effects on the practical realization of atomic frequency references is also discussed.

2 Theory

The following analysis applies to the three-level system shown in Figure 1a. Although the diagram addresses the

[a] e-mail: `levi@tf.ien.it`

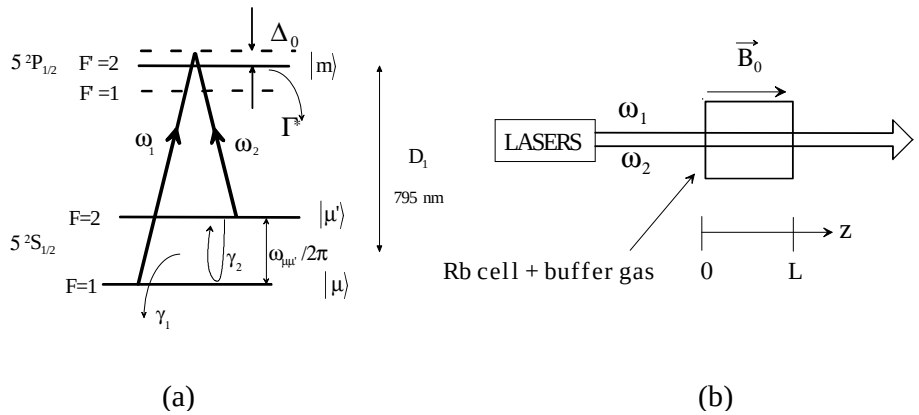

Fig. 1. Representation of the three energy levels scheme (a) and of the set-up (b) used in the theoretical analysis.

case of ^{87}Rb, it can be applied to the case of other alkali-metal atoms or to other closed three-level systems. The set-up considered in the theoretical analysis is illustrated in Figure 1b where the two laser beams are assumed to be collinear with the wave-vectors $\mathbf{k}_j = k_j\hat{\mathbf{z}}$ $(j = 1, 2)$.

We assume spatial variation of the field amplitudes only along the z-axis as well as a common polarization $\hat{\mathbf{e}}_\lambda$ independent of z, that is:

$$\mathbf{E}_j = E_j(z,t)\hat{\mathbf{e}}_\lambda; \quad \hat{\mathbf{e}}_\lambda \cdot \hat{\mathbf{z}} = 0; \quad \boldsymbol{\nabla} \cdot \mathbf{E}_j = 0 \qquad (j = 1, 2). \quad (1)$$

Some effects related to spatial variations of the field amplitudes in the directions normal to the wave vectors (laser beam profile) have been examined in [18] and are of minor interest in the present analysis. The amplitudes of the laser fields are assumed to be represented by:

$$E_j(z,t) = \frac{1}{2}\varepsilon_j(z,t)\mathrm{e}^{\mathrm{i}[\omega_j t - k_j z + \phi_j(z,t)]} + \text{c.c.} \qquad (j = 1, 2) \quad (2)$$

where ω_j is the angular frequency of the laser fields. In the analysis it is assumed that $\varepsilon_j(z,\, t)$ and $\phi_j(z,t)$ are slowly-variable functions of z and t, that is:

$$\begin{cases} \dfrac{\partial \varepsilon_j}{\partial t} \ll \omega_j \varepsilon_j, & \dfrac{\partial \varepsilon_j}{\partial z} \ll k_j \varepsilon_j \\ \dfrac{\partial \phi_j}{\partial t} \ll \omega_j, & \dfrac{\partial \phi_j}{\partial z} \ll k_j \end{cases} . \quad (3)$$

Equation (2) for the laser fields implies a strong correlation between the two radiation fields used in the Λ scheme. This condition can be ensured when these fields are provided by the first sidebands of a frequency or phase-modulated laser or by two phase-locked lasers with an offset frequency equal to the hyperfine separation.

At the operating temperatures mentioned in Section 1 and with N_2 as buffer gas which quenches partly the fluorescence emitted from the atomic ensemble, radiation trapping phenomena are mostly suppressed [19,20] and are not considered in the theory. The effect of the collisions between the buffer gas atoms and the alkali metal atoms is taken into account in:

(i) the relaxation rates γ_1 and γ_2 of the ground state hyperfine levels population difference and coherence respectively [21];
(ii) the decay rate of the excited state Γ^* [4] (nearly homogeneous broadening of $|m\rangle$);
(iii) the "localization" of the atoms on the microwave wavelength scale which cancels the Doppler effect through the Dicke effect [4,22].

The applied static magnetic field $\mathbf{B}_0$ provides a quantization axis and resolves the Zeeman levels in the ground state. The hyperfine level $F' = 2$ of the excited state is assumed to be the only excited state coupled by the optical fields and in the analysis we use the ideal three-level system shown in Figure 1a; in fact, the level $F' = 1$ in ^{87}Rb for example has a frequency separation from the $F' = 2$ level higher than the homogeneous width and a smaller Clebsh-Gordan coefficient. In Figure 1, the parameter Δ_0 is the laser detuning from the optical resonance.

The electric-dipole interaction of the laser radiation fields with the atomic ensemble is described by [21]:

$$\frac{\partial^2 E_j(z,t)}{\partial z^2} - \frac{1}{c^2}\frac{\partial^2 E_j(z,t)}{\partial t^2} = \mu_0 \frac{\partial^2 P_j(z,t)}{\partial t^2} \quad (4)$$

which is derived from Maxwell's equations for a homogeneous and isotropic medium. Analyzing the atomic system in the ensemble-averaged density matrix formalism [21], the polarization $P_j(z,t)$ in (4) may be expressed as:

$$P_j(z,t) = n\mathrm{Tr}(\hat{\boldsymbol{\rho}}\hat{\mathbf{P}}_j) \quad (5)$$

where n is the atomic density, $\hat{\boldsymbol{\rho}}$ and $\hat{\mathbf{P}}_j$ the density matrix and the polarization quantum operators respectively.

Assuming moreover a linear response of the atomic vapor, the polarization $P_j(z,t)$ is written as:

$$P_j(z,t) = \frac{1}{2}\mathcal{P}_j(z,t)\mathrm{e}^{\mathrm{i}[\omega_j t - k_j z + \phi_j(z,t)]} + \text{c.c.} \quad (6)$$

where $\mathcal{P}_j(z,t)$ is a complex function varying slowly with z and t:

$$\left|\frac{\partial \mathcal{P}_j}{\partial t}\right| \ll |\omega_j \mathcal{P}_j|, \quad \left|\frac{\partial \mathcal{P}_j}{\partial z}\right| \ll |k_j \mathcal{P}_j| \,. \quad (7)$$

Following a standard treatment (see for example [23]) and taking into account equations (3, 5, 6, 7), equations (4) may be reduced to the following set of first order partial differential equations:

$$\begin{cases} \dfrac{\partial\omega_{\mathrm{R1}}}{\partial z}+\dfrac{1}{c}\dfrac{\partial\omega_{\mathrm{R1}}}{\partial t}=\alpha_1\mathrm{Im}\delta_{\mu m} \\ \dfrac{\partial\phi_1}{\partial z}+\dfrac{1}{c}\dfrac{\partial\phi_1}{\partial t}=-\dfrac{\alpha_1}{\omega_{\mathrm{R1}}}\mathrm{Re}\delta_{\mu m} \\ \dfrac{\partial\omega_{\mathrm{R2}}}{\partial z}+\dfrac{1}{c}\dfrac{\partial\omega_{\mathrm{R2}}}{\partial t}=\alpha_2\mathrm{Im}\delta_{\mu' m} \\ \dfrac{\partial\phi_2}{\partial z}+\dfrac{1}{c}\dfrac{\partial\phi_2}{\partial t}=-\dfrac{\alpha_2}{\omega_{\mathrm{R2}}}\mathrm{Re}\delta_{\mu' m} \end{cases} \tag{8}$$

where we have introduced the Rabi angular frequencies,

$$\begin{cases} \omega_{\mathrm{R1}}=\varepsilon_1\langle\mu|e\,\hat{\mathbf{r}}\cdot\hat{\mathbf{e}}_\lambda|m\rangle/\hbar \\ \omega_{\mathrm{R2}}=\varepsilon_2\langle\mu'|e\,\hat{\mathbf{r}}\cdot\hat{\mathbf{e}}_\lambda|m\rangle/\hbar \end{cases} \tag{9}$$

the density parameters,

$$\begin{cases} \alpha_1=\dfrac{\omega_1\langle\mu|e\,\hat{\mathbf{r}}\cdot\hat{\mathbf{e}}_\lambda|m\rangle^2}{\varepsilon_0\hbar c}n \\ \alpha_2=\dfrac{\omega_2\langle\mu'|e\,\hat{\mathbf{r}}\cdot\hat{\mathbf{e}}_\lambda|m\rangle^2}{\varepsilon_0\hbar c}n \end{cases} \tag{10}$$

and the coherences density matrix elements in the form,

$$\begin{cases} \rho_{\mu\mu'}(z,t)=\delta_{\mu\mu'}(z,t)\mathrm{e}^{\mathrm{i}[(\omega_1-\omega_2)t-(k_1-k_2)z+\phi_1(z,t)-\phi_2(z,t)]} \\ \rho_{\mu m}(z,t)=\delta_{\mu m}(z,t)\mathrm{e}^{\mathrm{i}[\omega_1 t-k_1 z+\phi_1(z,t)]} \\ \rho_{\mu' m}(z,t)=\delta_{\mu' m}(z,t)\mathrm{e}^{\mathrm{i}[\omega_2 t-k_2 z+\phi_2(z,t)]} \end{cases}. \tag{11}$$

As usual, $\delta_{\mu m}$, $\delta_{\mu' m}$ and $\delta_{\mu\mu'}$ are slowly varying functions of z and t.

The evolution of the density matrix operator $\hat{\boldsymbol{\rho}}$ is given by the Liouville equation:

$$\frac{\partial\hat{\boldsymbol{\rho}}}{\partial t}=\frac{1}{\mathrm{i}\hbar}\left[\hat{\mathbf{H}},\hat{\boldsymbol{\rho}}\right]. \tag{12}$$

The rate equations obtained by means of equation (12) are made explicit in [4] and are valid also in the present case, taking into account equation (11). However, all the density matrix elements and the optical Rabi frequencies are functions of z. Due to the absence of a microwave cavity, there is no microwave field present and the microwave Rabi frequency is zero. In frequency standard applications, the laser interaction is always weak making $\omega_{\mathrm{R}j}\ll\Gamma^*$, $\forall z,t$ $(j=1,2)$. Consequently, the population of the excited state is small in comparison to that of the ground state. Taking into account all these considerations we obtain:

$$\begin{cases} \rho_{\mu\mu}+\rho_{\mu'\mu'}\approx 1 \\ \dot{\rho}_{mm}+\Gamma^*\rho_{mm}=-\omega_{\mathrm{R1}}\mathrm{Im}\delta_{\mu m}-\omega_{\mathrm{R2}}\mathrm{Im}\delta_{\mu' m} \\ \dot{\Delta}+\gamma_1\Delta=\omega_{\mathrm{R2}}\mathrm{Im}\delta_{\mu' m}-\omega_{\mathrm{R1}}\mathrm{Im}\delta_{\mu m} \\ \dot{\delta}_{\mu\mu'}+[\gamma_2+\mathrm{i}(\Omega_\mu+\dot{\phi}_1-\dot{\phi}_2)]\delta_{\mu\mu'}=\mathrm{i}\dfrac{\omega_{\mathrm{R1}}}{2}\delta_{m\mu'}-\mathrm{i}\dfrac{\omega_{\mathrm{R2}}}{2}\delta_{\mu m} \\ \dot{\delta}_{\mu m}+\left(\dfrac{1}{2}\Gamma^*+\mathrm{i}\Delta_0\right)\delta_{\mu m}=-\mathrm{i}\dfrac{\omega_{\mathrm{R1}}}{4}(1-\Delta)-\mathrm{i}\dfrac{\omega_{\mathrm{R2}}}{2}\delta_{\mu\mu'} \\ \dot{\delta}_{\mu' m}+\left(\dfrac{1}{2}\Gamma^*+\mathrm{i}\Delta_0\right)\delta_{\mu' m}=-\mathrm{i}\dfrac{\omega_{\mathrm{R2}}}{4}(1+\Delta)-\mathrm{i}\dfrac{\omega_{\mathrm{R1}}}{2}\delta_{\mu'\mu} \end{cases}. \tag{13}$$

In the above set of equations $\Delta=\rho_{\mu'\mu'}-\rho_{\mu\mu}$ is the population difference of the ground state hyperfine levels. $\Omega_\mu=(\omega_1-\omega_2)-\omega_{\mu'\mu}\ll\Gamma^*$ is the "microwave detuning", that is the detuning of the difference between the two radiation fields angular frequency and the ground state hyperfine angular frequency. The coupled sets of equations (8, 13) describe well an optically thick atomic sample under optical excitation in a Λ scheme. All the hypotheses done in developing the theory are widely satisfied in the usual experimental conditions. We are looking now for the steady-state solutions of the atomic ensemble $(\partial/\partial t\to 0)$. In that case the partial differential equations for ϕ_1 and ϕ_2 of (8) are uncoupled from the others. We consider the case for which $\Delta_0=0$, and the sets of equations (8, 13) reduce to:

$$\begin{cases} \rho_{mm}=\dfrac{\omega_{\mathrm{R1}}^2+\omega_{\mathrm{R2}}^2-\left(\omega_{\mathrm{R1}}^2-\omega_{\mathrm{R2}}^2\right)\Delta+4\omega_{\mathrm{R1}}\omega_{\mathrm{R2}}\mathrm{Re}\delta_{\mu\mu'}}{2\Gamma^{*2}} \\ \left[\gamma_1+\dfrac{\omega_{\mathrm{R1}}^2+\omega_{\mathrm{R2}}^2}{2\Gamma^*}\right]\Delta=\dfrac{\omega_{\mathrm{R1}}^2-\omega_{\mathrm{R2}}^2}{2\Gamma^*} \\ \left[\gamma_2+\dfrac{\omega_{\mathrm{R1}}^2+\omega_{\mathrm{R2}}^2}{2\Gamma^*}+\mathrm{i}\Omega_\mu\right]\delta_{\mu\mu'}=-\dfrac{\omega_{\mathrm{R1}}\omega_{\mathrm{R2}}}{2\Gamma^*} \\ \dfrac{\partial\omega_{\mathrm{R1}}}{\partial z}=-\dfrac{\alpha_1}{2\Gamma^*}\left[\omega_{\mathrm{R1}}(1-\Delta)+2\omega_{\mathrm{R2}}\mathrm{Re}\delta_{\mu\mu'}\right] \\ \dfrac{\partial\omega_{\mathrm{R2}}}{\partial z}=-\dfrac{\alpha_2}{2\Gamma^*}\left[\omega_{\mathrm{R2}}(1+\Delta)+2\omega_{\mathrm{R1}}\mathrm{Re}\delta_{\mu\mu'}\right] \end{cases}. \tag{14}$$

Before reporting and discussing the numerical solutions of the set of equations (14) which are of interest for the analysis of the experimental results reported below, it is instructive to consider the following particular case: (i) $\alpha_1\approx\alpha_2=\alpha$, a condition satisfied for the D_1 optical lines of alkali-metal atoms); (ii) $\omega_{\mathrm{R1}}(z=0)=\omega_{\mathrm{R2}}(z=0)=\omega_{\mathrm{R}}(0)$, equal laser intensities at the cell input. In that case the following analytical solution is found for (14):

$$\begin{cases} \Delta(z)=0 \quad \forall z\in[0,L] \\ \omega_{\mathrm{R1}}(z)=\omega_{\mathrm{R2}}(z)=\omega_{\mathrm{R}}(z) \quad \forall z\in[0,L] \\ \ln\dfrac{\omega_{\mathrm{R}}^2(z)}{\omega_{\mathrm{R}}^2(0)}+\dfrac{\omega_{\mathrm{R}}^2(0)}{\gamma_2\Gamma^*}\left[\dfrac{\omega_{\mathrm{R}}^2(z)}{\omega_{\mathrm{R}}^2(0)}-1\right]-\dfrac{\Omega_\mu^2}{\gamma_2^2} \\ \quad\times\ln\dfrac{\gamma_2^2+\Omega_\mu^2+\gamma_2\omega_{\mathrm{R}}^2(z)/\Gamma^*}{\gamma_2^2+\Omega_\mu^2+\gamma_2\omega_{\mathrm{R}}^2(0)/\Gamma^*}=-\dfrac{\alpha}{\Gamma^*}z \quad \forall z\in[0,L] \end{cases}. \tag{15}$$

The last equation of the set (15) has two asymptotic behaviors when $\Omega_\mu=0$:

$$\omega_{\mathrm{R}}^2(z)=\omega_{\mathrm{R}}^2(0)\mathrm{e}^{-\frac{\alpha}{\Gamma^*}z}, \qquad \omega_{\mathrm{R}}^2(0)/\Gamma^*\ll\gamma_2, \tag{16}$$

$$\omega_{\mathrm{R}}^2(z)=\omega_{\mathrm{R}}^2(0)\left[1-\frac{\alpha\gamma_2}{\omega_{\mathrm{R}}^2(0)}z\right], \quad \omega_{\mathrm{R}}^2(0)/\Gamma^*\gg\gamma_2. \tag{17}$$

Since $\omega_{\mathrm{R}}(z)$ is proportional to the optical field amplitude at position z, equation (16) represents the well-known classical Bouguer-Lambert-Beer attenuation law [24], while expression (17) gives the linear attenuation law typical of electromagnetically induced transparency [2].

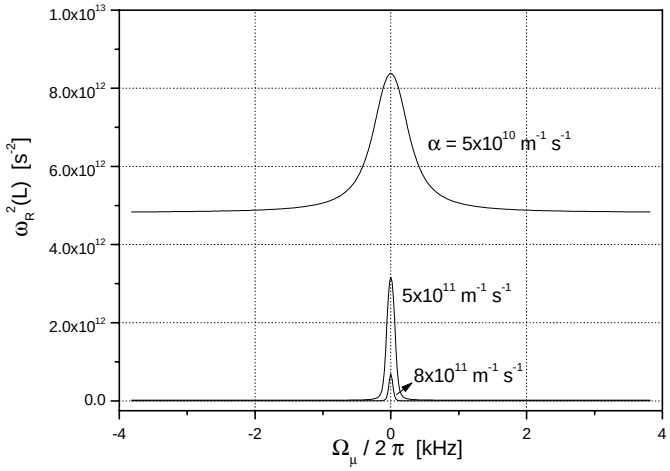

Fig. 2. Laser intensities transmitted at the end of the cell. In the vertical axis is reported $\omega_{\rm R}^2(L)$ obtained by the numerical integration of (14) for $L = 5$ cm, $\gamma_2 = 280$ s^{-1}, $\Gamma^* = 4 \times 10^9$ s^{-1} and $\omega_{\rm R1}(0) = \omega_{\rm R2}(0) = 3 \times 10^6$ s^{-1}. The parameter α is proportional to the atomic density (see text).

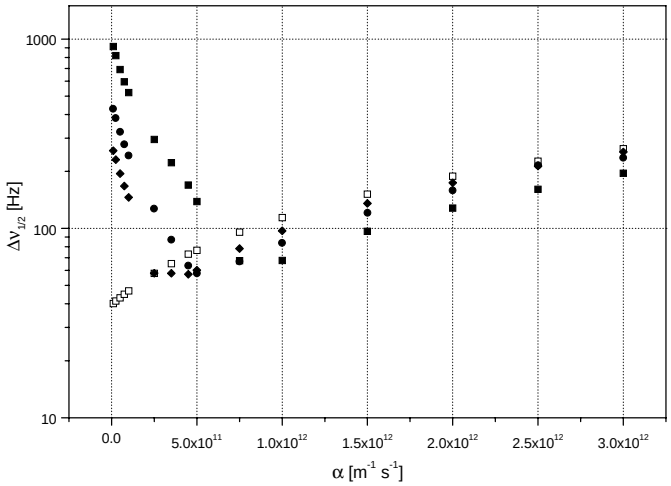

Fig. 3. Full width at half maximum of the light transmitted profile and ground state relaxation rate *versus* the atomic density represented by α: (■) $\omega_{\rm R}(0) = 3 \times 10^6$ s^{-1}; (●) $\omega_{\rm R}(0) = 2 \times 10^6$ s^{-1}; (♦) $\omega_{\rm R}(0) = 1.5 \times 10^6$ s^{-1}; (□) γ_2/π.

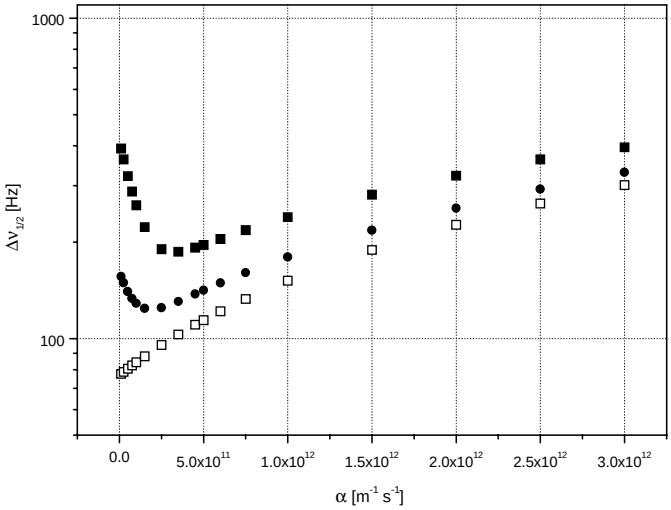

Fig. 4. Same as Figure 3 but now taking into account the real number of atoms in the ground state involving in the EIT process, as explained in the text: (■) $\omega_{\rm R}(0) = 2 \times 10^6$ s^{-1}; (●) $\omega_{\rm R}(0) = 1 \times 10^6$ s^{-1}; (□) γ_2/π.

The fluorescence intensity at position z is proportional to ρ_{mm} which is given by the first equation of set (14). This equation is uncoupled from the others of the same set and is used to calculate the fluorescence intensity. On the other hand, the Rabi frequency at the end of the cell containing the atomic ensemble is proportional to the laser field intensity at that position. The intensity of the light transmitted through the cell is thus evaluated from $\omega_{\rm R}^2(L)$. A typical result of the numerical evaluation of (15) is shown in Figure 2 for the transmitted power at the end of the cell; the numerical values of the parameters correspond to typical experimental conditions similar to those reported in the next section of this paper.

In particular, we assume for the electric-dipole moment a value of 2×10^{-29} C/m and the density parameter α for ^{87}Rb (^{133}Cs) is of the order of 5×10^{10} m^{-1} s^{-1} at 30 °C (14 °C) and 5×10^{11} m^{-1} s^{-1} at 50 °C (37 °C).

At exact resonance ($\Omega_\mu = 0$) the transmission is always maximum whatever α, a feature typical of the non-absorbing dark states due to the coherent population trapping in the ground state. Out of resonance an attenuation of the transmitted signal, much stronger than for the situation for which $\Omega_\mu = 0$ is predicted when the atomic density is increased, in agreement with the behaviors described by equations (16, 17). Moreover the transmission resonance line width decreases at higher densities, as reported also in [25–27] in quite different physical situations.

In particular, our calculations show that, in a pure three-level atomic system, the line width reduction in the transmission signal can achieve "sub-natural" level (that is smaller than γ_2) when the atomic density is increased above a certain value, as demonstrated in Figure 3 where we have also reported the ground state relaxation rate of Rb atoms in buffer gas.

However, our real atomic ensemble is not a pure three-level system but shows a Zeeman structure resolved by an applied static magnetic field. We take into account that the atoms involved in the EIT phenomenon are only those in $m_F = 0 - m_F = 0$, that means about 1/4 of the total atoms in the ground state for ^{87}Rb; then, we solved the system (14) introducing a density parameter $\alpha' = \alpha/4$ for the ground state atoms really excited by the coherent process. The last equations of (14) becomes:

$$\frac{\partial \omega_{\rm R}(z)}{\partial z} = -\frac{1}{2\Gamma^*}\omega_{\rm R}(z)[\alpha + 2\alpha' {\rm Re}\delta_{\mu\mu'}(z)]. \qquad (18)$$

The integration of the (18) shows that in this case, even if the atomic density is greatly increased, the line width of the emission profile stays always above the natural line width, as we can see in Figure 4.

The fluorescence signal (ρ_{mm}) computed from the set of equations (14) is reported in Figures 5 and 6 at two

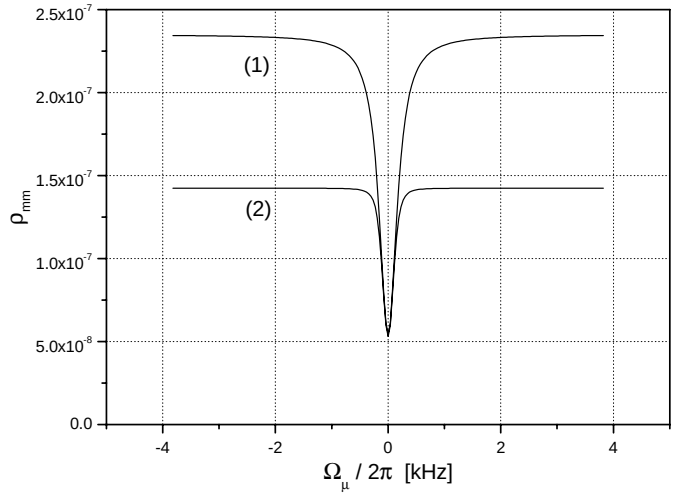

(a)

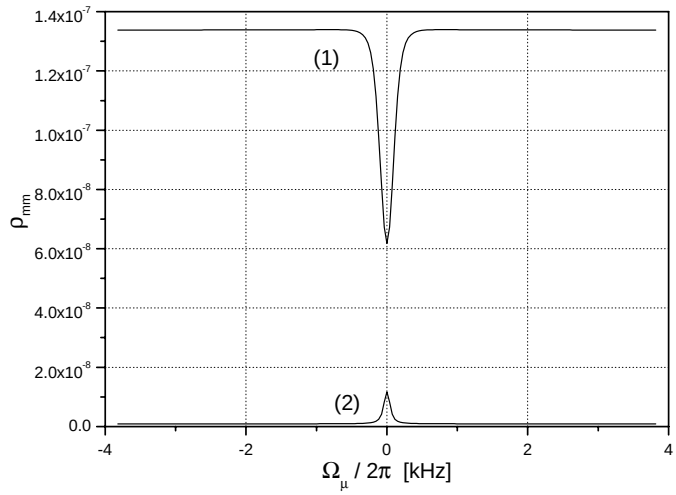

(b)

Fig. 5. Numerical solutions for ρ_{mm} (fluorescence signal); (1) $z = 5$ mm, (2) $z = 45$ mm; $\omega_{\mathrm{R1}}(0) = \omega_{\mathrm{R2}}(0) = 2 \times 10^6$ s^{-1}; $\Gamma^* = 4 \times 10^9$ s^{-1}; (a) $\gamma_2 = 280$ s^{-1}, $\alpha = 5 \times 10^{10}$ m^{-1} s^{-1} (values corresponding to 30 °C); (b) $\gamma_2 = 350$ s^{-1}, $\alpha = 5 \times 10^{11}$ m^{-1} s^{-1} (values corresponding to 60 °C).

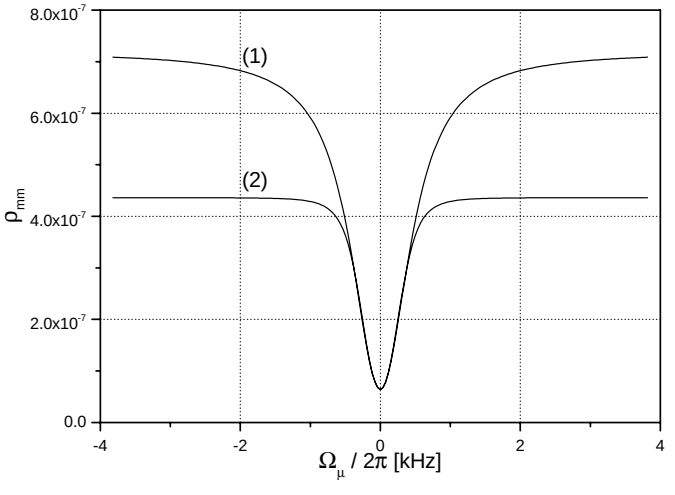

(a)

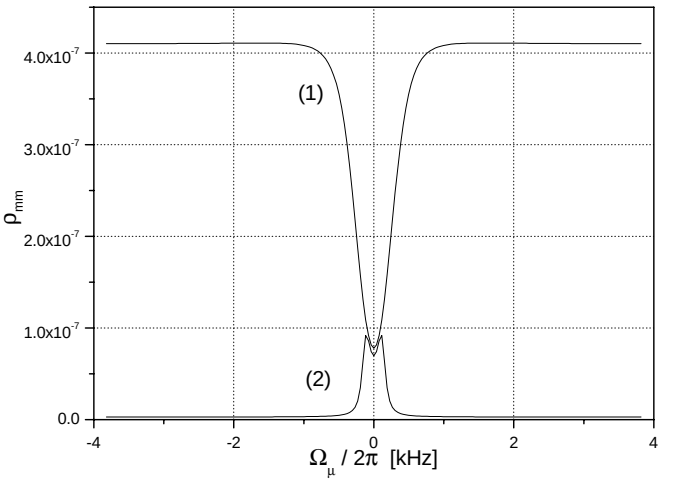

(b)

Fig. 6. Same as Figure 5 but for $\omega_{\mathrm{R1}}(0) = \omega_{\mathrm{R2}}(0) = 3.5 \times 10^6$ s^{-1}.

different positions, near the entrance and near the end of the cell, and for low and high atomic densities. In Figure 6 the laser intensities are three times higher then in Figure 5.

At low atomic density the dark line appears always as a reduction of the fluorescence signal, whatever the laser intensity and the position along z. Instead, at higher density, after a few cm of propagation in the atomic vapor, the fluorescence on resonance appears larger than the fluorescence off resonance. The dark line appears to be inverted looking like a bright line. This effect may be understood taking into account the two attenuation laws acting outside resonance (exponential) and near resonance (linear): the inverted dark line predicted in our computations is then an EIT effect which may be observed in the fluorescence spectrum. At high pumping rates the non-linearity presents in the differential equations of (14) produces more complicated resonance features as predicted in Figure 6b and observed in the experiments reported in the next section. In Figure 7 we report the 3D representations of the solutions of the system (14) for the fluorescence (Fig. 7a) and for the transmission signal (Fig. 7b) which make even more evident their behaviors described so far.

3 Experimental results

The experiments were done with the set-up shown in Figure 8. It consists of a laser diode operating at 795 nm

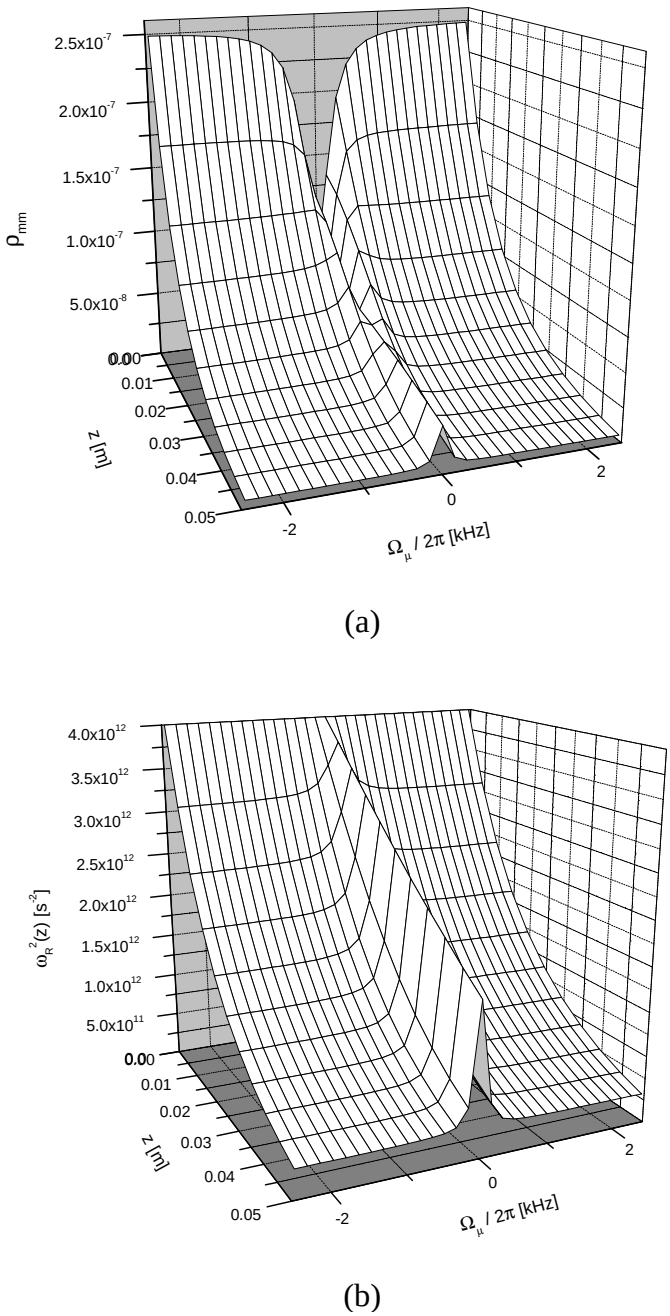

Fig. 7. 3D representation (a) of $\rho_{mm}(z)$ (fluorescence) and (b) of $\omega_{\mathrm{R}}^2(z)$ (transmission) as a function of distance within the cell *versus* the microwave detuning $\Omega_\mu/2\pi$, for $\Gamma = 4 \times 10^9$ s^{-1}, $\gamma_2 = 350$ s^{-1}, $\alpha = 3 \times 10^{11}$ m^{-1} s^{-1}, $\omega_{\mathrm{R}}(0) = 2 \times 10^6$ s^{-1}.

(D_1 transition of ^{87}Rb) and with a power output of about 10 mW; the laser is temperature controlled and coupled to an external cavity with a grating for tuning purposes; its line width is less than 1 MHz. The injection current of the laser diode is modulated at the angular frequency $\omega_m \approx \omega_{\mu'\mu}/2 = 2\pi \times 3.417$ GHz; the two first sidebands of the resulting frequency spectrum provide the two frequencies required for the Λ scheme interaction. In our experiments we achieve a frequency modulation index $m_{\mathrm{f}} \approx 2$. The residual unbalance between the amplitudes of the two sidebands is of the order of 10% and is due to the residual AM modulation.

The laser frequency is measured by means of a λ-meter while its spectrum is controlled with a Fabry-Perot interferometer through the monitor output shown in the figure. Saturated absorption is also monitored in a cell containing pure ^{87}Rb in order to control the laser carrier detuning Δ_0. The laser intensity is set through a variable neutral density filter while a $\lambda/4$ plate provides the σ^+ (or σ^-) polarization required to observe the $m_F = 0 - m_F = 0$ field independent microwave transition *via* the Λ scheme [18]. The laser beam profile is Gaussian with a 1/e diameter of $\approx$1 cm.

The quartz cell 5 cm long and 2 cm in diameter is enclosed in a copper cylinder acting as a holding structure and as an oven for controlling the temperature and the atomic density of the alkali metal vapor. The cell contains pure ^{87}Rb and a mixture of buffer gases consisting of 10 torr of N_2 and 15 torr of Ar, providing partial temperature compensation.

A pair of Helmholtz coils, which generate a static magnetic field of 100 mG, provides the axis of quantization. Finally three diodes are used to detect the transmitted laser intensity and the fluorescence not fully quenched by N_2 at the entrance and at the end of the cell through holes with a diameter of 2 mm.

The experimental results reported in the following figures refer to 30 °C and 50 °C; in this temperature range and with the total buffer gas pressure of 25 torr, we have $\Gamma^* \approx 4 \times 10^9$ s^{-1}, $\gamma_1 \approx \gamma_2$, $\gamma_2 \approx 280$ s^{-1} at 30 °C and $\gamma_2 \approx 350$ s^{-1} at 50 °C [21].

The dark line at low atomic density is shown in Figure 9a as observed in the fluorescence spectrum, near the entrance and at the end of the cell. The transmission signal is also shown under the same conditions. The well-known non-absorbing behavior of the CPT phenomenon is made evident. The fluorescence signal at the cell entrance corresponds to an optically thin medium. Using the analysis made in reference [5] and the measured line width, the optical Rabi frequency, $\omega_{\mathrm{R}}(0)$, is estimated to be of the order of 1.5×10^6 s^{-1}, valid for all the records of Figure 9. The pumping rate $\omega_{\mathrm{R}}^2(0)/\Gamma^*$ is then of the order of 500 s^{-1}.

At a temperature of 50 °C, the medium is no longer optically thin and an inverted dark line is observed near the end of the cell as reported in Figure 9b in excellent agreement with the theoretical predictions (Fig. 5b). The pumping rate, however, is not large enough to lead to a decrease of the transmission resonance line width when the atomic density is increased. The experimental results shown in Figure 10 are obtained for the same conditions as those of Figure 9 but with a pumping rate $\omega_{\mathrm{R}}^2(0)/\Gamma^* \approx 2\,000$ s^{-1}. The more complicated structure of the inverted dark line in Figure 10b agrees qualitatively with the computation reported in Figure 6b. The asymmetries observed in the dark line profiles at the cell entrance are due to the sidebands unbalance of the laser spectrum with a laser carrier detuning $\Delta_0/2\pi \approx 100$ MHz, as demonstrated in [4,18].

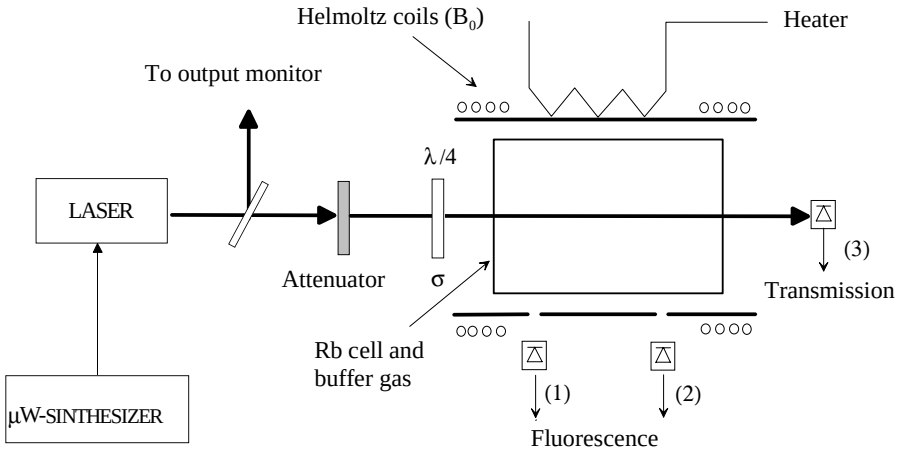

Fig. 8. Experimental arrangement used to observe the dark line in the fluorescence spectrum (photodetectors (1) and (2)) and the bright line in the transmitted radiation (photodetector (3)).

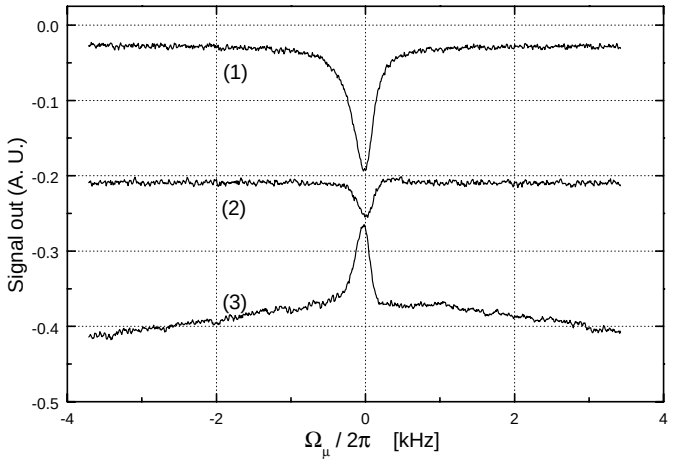

(a)

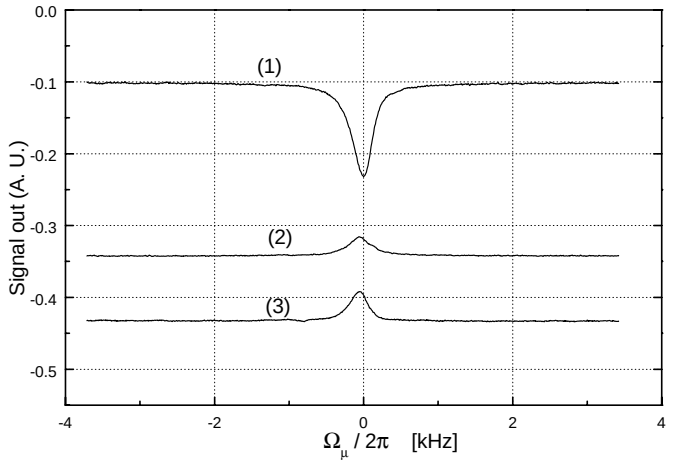

(b)

Fig. 9. Experimental behaviors of fluorescence and transmission signals for a pumping rate of 500 s^{-1}; (a) 30 °C and (b) 50 °C. (1) et (2) refer to the photodetectors for the detection of the fluorescence and (3) refers to the photodetector for the detection of the transmitted light, as also indicated in Figure 8.

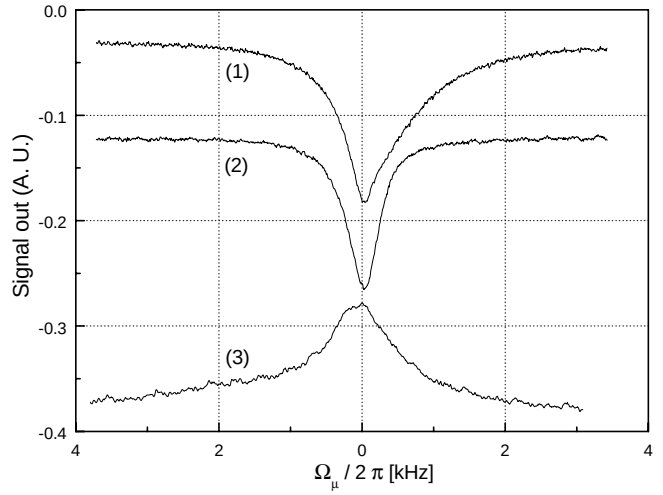

(a)

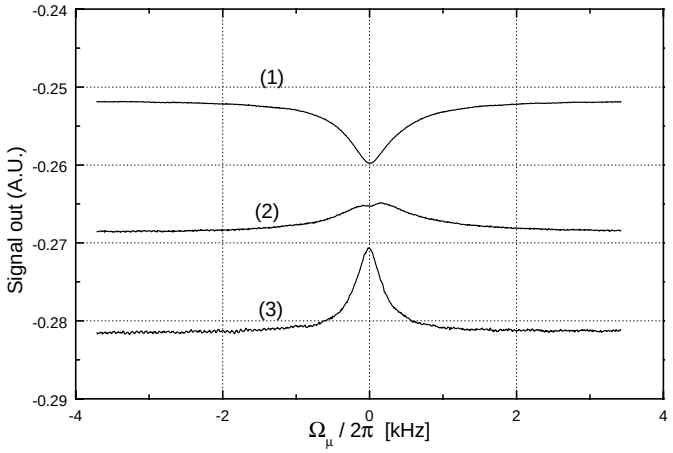

(b)

Fig. 10. Same as Figure 9 but for a pumping rate of 2 000 s^{-1}; (a) 30 °C and (b) 50 °C.

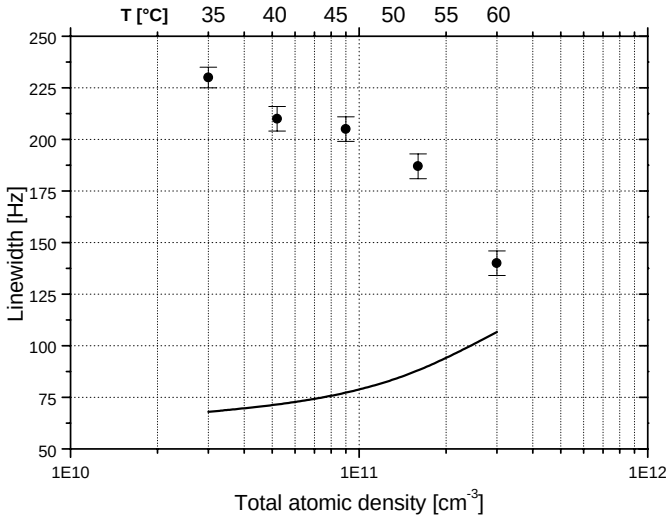

Fig. 11. Experimental measurements of the line width reduction in ^{87}Rb *versus* atomic density (•). The natural line width is obtained by the value of γ_2 (—); $\omega_{\rm R}(0)$ is of the order of 1.5×10^6 s^{-1}.

The line width reduction of the transmission resonance signal at 50 °C is evident, in agreement with the computations reported in Figure 2. Moreover, we have also measured the line width reduction as an atomic density function; the results of Figure 11 are in good quantitative agreement with theoretical prediction previously reported (Fig. 4). The line width behavior against the temperature is not understood with the theory developed for a thin medium, where an increase of the coherence relaxation ratio γ_2 would lead to a line width broadening, while it is correctly predicted if the atomic density is taken into account.

We have also performed analogous experiments with many cells 4 cm long and 4 cm in diameter containing ^{133}Cs and various buffer gases (see [4]). An inversion of the fluorescence dark line was always observed for $T \gtrsim 30$ °C, where the sample behaves as a thick vapor for temperature lower than in the case of Rb.

Finally, we have also done RF-optical double resonance experiments in ^{87}Rb and in ^{133}Cs thick vapors in which the optical pumping was done with a laser. The optical excitation mechanism involved is often called intensity optical pumping. It is used in the study of passive frequency standards in which a laser is used for the optical pumping instead of a spectral lamp. In that case also, we have observed inverted fluorescence signals while in transmission the resonance line remained always an absorption line. This phenomenon is readily explained in terms of the analysis made above, since the configuration corresponds to a "ladder scheme" (or a "V-scheme" if the pumping is done from the lower ground state level), a scheme which has been studied extensively [6,10].

We do not expand on these last experiments since they do not add new insight on the physics involved in CPT in optically thick media. However, they confirm that the analysis reported in the present paper can be extended readily to more general closed three-level systems driven by means of coherent fields.

4 Discussion and conclusions

The analysis and experimental results reported in the present paper show that optically thick vapors alter considerably the nature of the signals observed in Coherent Population Trapping experiments. It was shown that in alkali metal atom vapors at moderately high atomic densities ($n \sim 10^{11}$ cm^{-3}), an inverted dark line is observed in the fluorescence spectrum. The importance of this inversion depends on the position of observation along the propagation direction of the laser beam. The effect is caused by non-linear absorption within the ensemble, which acts differently for the conditions on- resonance and off-resonance. This effect is also responsible for the phenomenon called electromagnetically induced transparency observed in such systems (EIT).

Analogous inversion phenomena are also observed for the ladder scheme corresponding to the RF-optical double resonance widely used in frequency standards investigations using laser optical pumping. In these applications, the fluorescence signal may not be useful due to its undesirable reversal feature at high densities.

We have also shown that the CPT transmission resonance line remains bright in optically thick vapors. Besides, the possibility to attain narrow line width (even below the natural line width for a pure three level atomic system) is predicted; this feature could be of interest in frequency standard applications, giving the opportunity to obtain resonance with a high quality factor, a good signal-to-noise ratio and with a strong reduction of the background signal.

The authors wish to thank N. Beverini and E. Maccioni for their help in filling the cells with rubidium, cesium and the appropriate buffer gases. This work has been partially supported by ASI (Italian Space Agency).

References

1. G. Alzetta, A. Gozzini, L. Moi, G. Orriols, Nuovo Cimento B **36**, 5 (1976).
2. K.J. Boller, A. Imamoglu, S.E. Harris, Phys. Rev. Lett. **66**, 2593 (1991).
3. A. Godone, F. Levi, J. Vanier, Phys. Rev. A **59**, R12 (1999).
4. J. Vanier, A. Godone, F. Levi, Phys. Rev. A **58**, 2345 (1998).
5. G. Orriols, Nuovo Cimento **53**, 1 (1979).
6. E. Arimondo, Progr. Opt. **XXXV**, 257 (1996).
7. R. Wynands, A. Nagel, Appl. Phys. B **68**, 1 (1999).
8. H. Lee, M. Fleischauer, M.O. Scully, Phys. Rev. A **58**, 2587 (1998).
9. A. Aspect, E. Arimondo, R. Kaiser, N. Vansteenkiste, C. Cohen-Tannoudji, JOSA B **11**, 2112 (1989).
10. M.O. Scully, Phys. Rep. **219**, 191 (1992).

11. N. Cyr, M. Têtu, M. Breton, IEEE Trans. IM **42**, 640 (1993).
12. A. Godone, F. Levi, J. Vanier, IEEE Trans. UFFC **46**, 609 (1999).
13. J. Kitching, S. Kuappe, N. Vukicevic, L. Hollberg, R. Wynands, W. Weidemann, IEEE Trans. IM Vol. 49, p.1313-1317, Issue 6.
14. E.A. Korunsky, Kosachiov, Phys. Rev. A **60**, 4996 (1999).
15. A.M. Akulshin, S. Barreiro, A. Lezana, Phys. Rev. Lett. **83**, 4277 (1999).
16. F. Levi, A. Godone, J. Vanier, IEEE Trans. UFFC **47**, 466 (2000).
17. A. Godone, F. Levi, S. Micalizio, J. Vanier, Phys. Rev. A **62**, 053402 (2000).
18. F. Levi, A. Godone, J. Vanier, S. Micalizio, G. Modugno, Eur. Phys. J. D **12**, 53 (2000).
19. J.C. Camparo, JOSA B **15**, 1177 (1998).
20. M. Fleischauer, Europhys. Lett. **45**, 659, (1999).
21. J. Vanier, C. Audoin, *The Quantum Physics of Atomic Frequency Standards* (Adam Hilger, Bristol, 1989).
22. R.H. Dicke, Phys. Rev. **89**, 472 (1953).
23. M.O. Scully, M.S. Zubairy, *Quantum Optics* (Cambridge University Press, Cambridge, 1999).
24. D. Kosachiov, Quant. Electron. **25**, 1089 (1995).
25. M.D. Lukin, M. Fleischauer, A.S. Zibrov, H.G. Robinson, V.L. Velichansky, L. Hollberg, M.O. Scully, Phys. Rev. Lett. **79**, 2959 (1997).
26. C.L. Bentley Jr, J. Liu, Y. Liao, Phys. Rev. A **61**, 023811 (2000).
27. L. Cayan, S. Kroll, L. Sturesson, S. Svanberg, Phys. Rev. A **53**, 1668 (1996).